Biomedical Optics EXPRESS

# Spatial sensitivity and penetration depth of three cerebral oxygenation monitors

**Sonny Gunadi, Terence S. Leung, Clare E. Elwell, and Ilias Tachtsidis***

*Department of Medical Physics and Biomedical Engineering, University College London, Gower Street, London, WC1E 6BT, UK*

*i.tachtsidis@ucl.ac.uk

**Abstract:** The spatial sensitivities of NIRO-100, ISS Oximeter and TRS-20 cerebral oxygenation monitors are mapped using the local perturbation method to inform on their penetration depths and susceptibilities to superficial contaminations. The results show that TRS-20 has the deepest mean penetration depth and is less sensitive than the other monitors to a localized absorption change in the superficial layer. However, an integration time of more than five seconds is required by the TRS-20 to achieve an acceptable level of signal-to-noise ratio, which is the poorest amongst the monitors. With the exception of NIRO-100 continuous wave method, the monitors are not significantly responsive to layer-wide absorption change that occurs in the superficial layer.



**OCIS codes:** (170.0170) Medical optics and biotechnology; (170.3890) Medical optics instrumentation; (170.3660) Light propagation in tissues.

## References and links

1. M. Wolf, M. Ferrari, and V. Quaresima, "Progress of near-infrared spectroscopy and topography for brain and muscle clinical applications," J. Biomed. Opt. **12**(6), 062104 (2007).
2. M. Ferrari and V. Quaresima, "A brief review on the history of human functional near-infrared spectroscopy (fNIRS) development and fields of application," Neuroimage **63**(2), 921–935 (2012).
3. S. Lloyd-Fox, A. Blasi, and C. E. Elwell, "Illuminating the developing brain: The past, present and future of functional near infrared spectroscopy," Neurosci. Biobehav. Rev. **34**(3), 269–284 (2010).
4. F. Scholkmann, S. Kleiser, A. J. Metz, R. Zimmermann, J. Mata Pavia, U. Wolf, and M. Wolf, "A review on continuous wave functional near-infrared spectroscopy and imaging instrumentation and methodology," Neuroimage **85**(Pt 1), 6–27 (2014).
5. C. E. Elwell and C. E. Cooper, "Making light work: Illuminating the future of biomedical optics," Philos. Trans. R. Soc., A **369**(1955), 4358–4379 (2011).
6. A. Torricelli, D. Contini, A. Pifferi, M. Caffini, R. Re, L. Zucchelli, and L. Spinelli, "Time domain functional NIRS imaging for human brain mapping," Neuroimage **85**(Pt 1), 28–50 (2014).
7. E. Okada and D. T. Delpy, "Near-infrared light propagation in an adult head model. II. Effect of superficial tissue thickness on the sensitivity of the near-infrared spectroscopy signal," Appl. Opt. **42**(16), 2915–2922 (2003).
8. D. A. Boas and A. M. Dale, "Simulation study of magnetic resonance imaging-guided cortically constrained diffuse optical tomography of human brain function," Appl. Opt. **44**(10), 1957–1968 (2005).
9. E. Kirilina, A. Jelzow, A. Heine, M. Niessing, H. Wabnitz, R. Brühl, B. Ittermann, A. M. Jacobs, and I. Tachtsidis, "The physiological origin of task-evoked systemic artefacts in functional near infrared spectroscopy," Neuroimage **61**(1), 70–81 (2012).
10. S. Fantini, M.-A. Franceschini, J. S. Maier, S. A. Walker, B. B. Barbieri, and E. Gratton, "Frequency-domain multichannel optical detector for noninvasive tissue spectroscopy and oximetry," Opt. Eng. **34**(1), 32–42 (1995).
11. D. T. Delpy, M. Cope, P. van der Zee, S. Arridge, S. Wray, and J. Wyatt, "Estimation of optical pathlength through tissue from direct time of flight measurement," Phys. Med. Biol. **33**(12), 1433–1442 (1988).
12. S. Suzuki, S. Takasaki, T. Ozaki, and Y. Kobayashi, "Tissue oxygenation monitor using NIR spatially resolved spectroscopy," Proc. SPIE **3597**, 582–592 (1999).
13. M. S. Patterson, B. Chance, and B. C. Wilson, "Time resolved reflectance and transmittance for the non-invasive measurement of tissue optical properties," Appl. Opt. **28**(12), 2331–2336 (1989).
14. S. Fantini, D. Hueber, M. A. Franceschini, E. Gratton, W. Rosenfeld, P. G. Stubblefield, D. Maulik, and M. R. Stankovic, "Non-invasive optical monitoring of the newborn piglet brain using continuous-wave and frequency-domain spectroscopy," Phys. Med. Biol. **44**(6), 1543–1563 (1999).

#212653 - $15.00 USD Received 23 May 2014; revised 16 Jul 2014; accepted 16 Jul 2014; published 1 Aug 2014

15. D. A. Boas, A. M. Dale, and M. A. Franceschini, “Diffuse optical imaging of brain activation: Approaches to optimizing image sensitivity, resolution, and accuracy,” Neuroimage **23**(Suppl 1), S275–S288 (2004).
16. W. Cui, C. Kumar, and B. Chance, “Experimental study of migration depth for the photons measured at sample surface,” Proc. SPIE **1431**, 180–191 (1991).
17. N. C. Bruce, “Experimental study of the effect of absorbing and transmitting inclusions in highly scattering media,” Appl. Opt. **33**(28), 6692–6698 (1994).
18. A. V. Patil, J. Safaie, H. A. Moghaddam, F. Wallois, and R. Grebe, “Experimental investigation of NIRS spatial sensitivity,” Biomed. Opt. Express **2**(6), 1478–1493 (2011).
19. T. Vaithianathan, I. D. C. Tullis, N. Everdell, T. Leung, A. Gibson, J. Meek, and D. T. Delpy, “Design of a portable near infrared system for topographic imaging of the brain in babies,” Rev. Sci. Instrum. **75**(10), 3276–3283 (2004).
20. S. Gunadi and T. S. Leung, “Spatial Sensitivity of Acousto-Optic and Optical Near-Infrared Spectroscopy Sensing Measurements,” J. Biomed. Opt. **16**(12), 127005 (2011).
21. S. R. Arridge, “Photon-measurement density functions. Part I: Analytical forms,” Appl. Opt. **34**(31), 7395–7409 (1995).
22. L. H. Wang, S. L. Jacques, and X. M. Zhao, “Continuous-Wave Ultrasonic Modulation of Scattered Laser Light to Image Objects in Turbid Media,” Opt. Lett. **20**(6), 629–631 (1995).
23. S. Del Bianco, F. Martelli, and G. Zaccanti, “Penetration depth of light re-emitted by a diffusive medium: Theoretical and experimental investigation,” Phys. Med. Biol. **47**(23), 4131–4144 (2002).
24. S. J. Matcher, P. J. Kirkpatrick, K. Nahid, M. Cope, and D. T. Delpy, “Absolute quantification methods in tissue near-infrared spectroscopy,” Proc. SPIE **2389**, 486–495 (1995).
25. M. Oda, Y. Yamashita, T. Nakano, A. Suzuki, K. Shimizu, I. Hirano, F. Shimomura, E. Ohmae, T. Suzuki, and Y. Tsuchiya, “Near-infrared time-resolved spectroscopy system for tissue oxygenation monitor,” Proc. SPIE **4160**, 204–210 (2000).
26. K. Yoshitani, K. Kuwajima, T. Irie, Y. Inatomi, A. Miyazaki, K. Iihara, and Y. Ohnishi, “Clinical validity of cerebral oxygen saturation measured by time-resolved spectroscopy during carotid endarterectomy,” J. Neurosurg. Anesthesiol. **25**(3), 248–253 (2013).
27. S. T. Flock, S. L. Jacques, B. C. Wilson, W. M. Star, and M. J. C. van Gemert, “Optical properties of Intralipid: A phantom medium for light propagation studies,” Lasers Surg. Med. **12**(5), 510–519 (1992).
28. H. J. van Staveren, C. J. M. Moes, J. van Marie, S. A. Prahl, and M. J. C. van Gemert, “Light scattering in Intralipid-10% in the wavelength range of 400-1100 nm,” Appl. Opt. **30**(31), 4507–4514 (1991).
29. M. Firbank, M. Oda, and D. T. Delpy, “An improved design for a stable and reproducible phantom material for use in near-infrared spectroscopy and imaging,” Phys. Med. Biol. **40**(5), 955–961 (1995).
30. A. Duncan, J. H. Meek, M. Clemence, C. E. Elwell, L. Tyszczuk, M. Cope, and D. T. Delpy, “Optical pathlength measurements on adult head, calf and forearm and the head of the newborn infant using phase resolved optical spectroscopy,” Phys. Med. Biol. **40**(2), 295–304 (1995).
31. S. J. Matcher, M. Cope, and D. T. Delpy, “Use of the water absorption spectrum to quantify tissue chromophore concentration changes in near-infrared spectroscopy,” Phys. Med. Biol. **39**(1), 177–196 (1994).
32. Y. Ueda, K. Yoshimoto, E. Ohmae, T. Suzuki, T. Yamanaka, D. Yamashita, H. Ogura, C. Teruya, H. Nasu, E. Ima, H. Sakahara, M. Oda, and Y. Yamashita, “Time-resolved optical mammography and its preliminary clinical results,” Technol. Cancer Res. Treat. **10**(5), 393–401 (2011).
33. K. Suzuki, Y. Yamashita, K. Ohta, and B. Chance, “Quantitative measurement of optical parameters in the breast using time-resolved spectroscopy. Phantom and preliminary in vivo results,” Invest. Radiol. **29**(4), 410–414 (1994).
34. J. Selb, J. J. Stott, M. A. Franceschini, A. G. Sorensen, and D. A. Boas, “Improved sensitivity to cerebral hemodynamics during brain activation with a time-gated optical system: analytical model and experimental validation,” J. Biomed. Opt. **10**(1), 011013 (2005).
35. E. Ohmae, Y. Ouchi, M. Oda, T. Suzuki, S. Nobesawa, T. Kanno, E. Yoshikawa, M. Futatsubashi, Y. Ueda, H. Okada, and Y. Yamashita, “Cerebral hemodynamics evaluation by near-infrared time-resolved spectroscopy: Correlation with simultaneous positron emission tomography measurements,” Neuroimage **29**(3), 697–705 (2006).
36. T. Correia, A. Gibson, and J. Hebden, “Identification of the optimal wavelengths for optical topography: a photon measurement density function analysis,” J. Biomed. Opt. **15**(5), 056002 (2010).
37. L. Zucchelli, D. Contini, R. Re, A. Torricelli, and L. Spinelli, “Method for the discrimination of superficial and deep absorption variations by time domain fNIRS,” Biomed. Opt. Express **4**(12), 2893–2910 (2013).
38. L. Gagnon, M. A. Yücel, D. A. Boas, and R. J. Cooper, “Further improvement in reducing superficial contamination in NIRS using double short separation measurements,” Neuroimage **85**(Pt 1), 127–135 (2014).
39. P. G. Al-Rawi, P. Smielewski, and P. J. Kirkpatrick, “Evaluation of a near-infrared spectrometer (NIRO 300) for the detection of intracranial oxygenation changes in the adult head,” Stroke **32**(11), 2492–2500 (2001).
40. S. Powell and T. S. Leung, “Highly parallel Monte-Carlo simulations of the acousto-optic effect in heterogeneous turbid media,” J. Biomed. Opt. **17**(4), 045002 (2012).
41. J. C. Hebden and S. R. Arridge, “Imaging through scattering media by the use of an analytical model of perturbation amplitudes in the time domain,” Appl. Opt. **35**(34), 6788–6796 (1996).
42. A. Knüttel, J. M. Schmitt, and J. R. Knutson, “Spatial localization of absorbing bodies by interfering diffusive photon-density waves,” Appl. Opt. **32**(4), 381–389 (1993).

#212653 - $15.00 USD Received 23 May 2014; revised 16 Jul 2014; accepted 16 Jul 2014; published 1 Aug 2014

43. L. Spinelli, F. Martelli, S. Del Bianco, A. Pifferi, A. Torricelli, R. Cubeddu, and G. Zaccanti, "Absorption and scattering perturbations in homogeneous and layered diffusive media probed by time-resolved reflectance at null source-detector separation," Phys. Rev. E Stat. Nonlin. Soft Matter Phys. **74**(2), 021919 (2006).
44. A. Torricelli, A. Pifferi, L. Spinelli, R. Cubeddu, F. Martelli, S. Del Bianco, and G. Zaccanti, "Time-resolved reflectance at null source-detector separation: Improving contrast and resolution in diffuse optical imaging," Phys. Rev. Lett. **95**(7), 078101 (2005).
45. R. Esposito, F. Martelli, and S. De Nicola, "Closed-form solution of the steady-state photon diffusion equation in the presence of absorbing inclusions," Opt. Lett. **39**(4), 826–829 (2014).
46. A. Jelzow, H. Wabnitz, I. Tachtsidis, E. Kirilina, R. Brühl, and R. Macdonald, "Separation of superficial and cerebral hemodynamics using a single distance time-domain NIRS measurement," Biomed. Opt. Express **5**(5), 1465–1482 (2014).
47. G. Strangman, J. P. Culver, J. H. Thompson, and D. A. Boas, "A quantitative comparison of simultaneous BOLD fMRI and NIRS recordings during functional brain activation," Neuroimage **17**(2), 719–731 (2002).
48. T. J. Huppert, R. D. Hoge, S. G. Diamond, M. A. Franceschini, and D. A. Boas, "A temporal comparison of BOLD, ASL, and NIRS hemodynamic responses to motor stimuli in adult humans," Neuroimage **29**(2), 368–382 (2006).
49. J. Selb, T. M. Ogden, J. Dubb, Q. Fang, and D. A. Boas, "Comparison of a layered slab and an atlas head model for Monte Carlo fitting of time-domain near-infrared spectroscopy data of the adult head," J. Biomed. Opt. **19**(1), 016010 (2014).
50. L. Gagnon, C. Gauthier, R. D. Hoge, F. Lesage, J. Selb, and D. A. Boas, "Double-layer estimation of intra- and extracerebral hemoglobin concentration with a time-resolved system," J. Biomed. Opt. **13**(5), 054019 (2008).

## 1. Introduction

The adoption of near infrared spectroscopy (NIRS) in clinics for non-invasive muscle and cerebral oxygenation monitoring has been growing for both adults and infants [1–6]. NIRS exploits the low light absorption of human tissue in the near infrared (NIR) region between 650 and 950 nm. The absorption spectra of oxy- and deoxygenated hemoglobins are distinct, thus their concentrations can be resolved.

In cerebral oxygenation monitoring, the cortex lies in a region beneath the scalp, skull and a layer of cerebral spinal fluid (CSF), which are often referred to as the superficial layers (SPL). It has been shown in computer simulations that NIRS can be more sensitive to absorption changes in the SPL than in the deeper regions [7, 8]. Experimental studies also confirm that hemodynamic changes in the scalp can contaminate cerebral measurement [9, 10]. The level and/or presence of contamination largely depend on the NIRS method adopted by the NIRS systems. Details of NIRS monitors in the market and their usage in clinical research are available [1, 2, 4, 6]; these monitors are typically categorized into continuous wave (CW) [4, 11], spatially resolved [12], time-domain (TD) [6, 13] and frequency domain (FD) [14]. The reconstruction accuracy of the oxygenation measurement, and computer simulation validations of these methods are well discussed in the literature [4, 6, 15]. In this paper, the regional sensitivity of the NIRS cerebral oxygenation monitors is investigated. This assessment covers both the instrumentation and the adopted NIRS method to derive oxygenation measurements in their respective normal operating modes. The ideal monitor would have 100% sensitivity in the brain and 0% sensitivity in the SPL.

The regional sensitivity of NIRS monitors for cerebral tissue oxygenation measurement can be assessed in two areas. Firstly, how deep the monitors can measure; the cortex is located beneath layers of scalp, skull and CSF, thus a large penetration depth is essential in accurate monitoring of the brain. Secondly, how sensitive the monitors are to optical property changes in SPL, which also affects the accuracy of measurement. One established method to map the spatial sensitivity and determine the mean penetration depth of NIRS measurement is the local perturbation method [16]. By using the local perturbation method, Cui et al. [16] experimentally measured the spatial sensitivity map in reflection mode in a turbid medium that resembled a 'banana' shape profile. The spatial sensitivity is defined as the amount of an absorption change or light attenuation change detected by the NIRS monitor in response to a localized absorption change in a particular location within a turbid medium. A sensitivity map can be formed by systematically relocating the local absorber throughout a predefined scanning area within a diffuse medium and recording the changes in measurements

#212653 - $15.00 USD Received 23 May 2014; revised 16 Jul 2014; accepted 16 Jul 2014; published 1 Aug 2014

accordingly [17–20]. This experimental method of spatial sensitivity mapping by local perturbation is similar to the sensitivity profile [8] or the photon measurement density function (PMDF) [21] used in computer simulation of light transport to inform on the regional sensitivity of measurement.

In our previous investigation [20], we compared the spatial sensitivity maps and mean penetration depths of two NIRS methods and acousto-optic (AO) sensing for transmittance and reflectance measurements. The NIRS methods were a CW single source-detector (SSD) method and a spatially resolved spectroscopy (SRS) method. The AO method [22] uses focused ultrasound field to label photons that propagate through the ultrasound field. By measuring the ultrasound modulated intensity, a localized measurement can be obtained. The results showed that all methods were sensitive to localized absorption changes in SPL, especially when these changes occurred in close proximity to the optical source and detector. The SSD method had the shallowest mean penetration depth, followed by SRS and AO. However, there are differences in the experimental setup used in the previous study and this paper, which will be discussed later.

The aim of this study is to assess the spatial and depth sensitivities of three NIRS cerebral oxygenation monitors operating under their respective normal mode and using the manufacturer supplied optical probes. Each monitor employs a different NIRS method and uses a different optical source-detector separation to derive oxygenation measurements. As discussed extensively in the literature [4, 6, 15, 18, 23] source-detector separation can have a direct effect on the sensitivity, penetration depth and signal to noise ratio of the measurement; however this has not been investigated here in the context of comparison between different instruments. The oxygenation monitors that we investigated are: (1) the NIRO-100 (Hamamatsu Photonics K.K.) that operates in CW mode and utilizes SRS to derive the absolute tissue oxygen saturation ($S_tO_2$) [12, 24]; (2) the ISS Oximeter (Model 96208, ISS Inc.) [10, 14] that operates in the FD domain mode and applies the multi-distance FD method; and (3) the TRS-20 (Hamamatsu Photonics K.K.) [25, 26] that is based on the TD method. In this study their spatial sensitivity maps are measured to assess their responses to highly localized absorption coefficient ($\mu_a$) changes. The amount of absorption or light attenuation change measured by each system with and without the localized absorption is used to derive the sensitivity. In addition, we calculate and present their mean sensitivities to inform on the depth penetration, which can also be regarded to represent a layer-wide sensitivity at different depths. Subsequently we derive and present the mean penetration depth of each monitor.

## 2. Materials and methods

### *2.1. Experimental setup and phantoms*

The monitors were set to operate in their respective normal operation mode for reflectance absorption measurement using their default optical source and detector separations. The monitors were also set to use the same integration time of two seconds. We chose two seconds as the integration time because it was a reasonable compromise between improved signal-to-noise ratio and a sufficient temporal resolution to monitor most of physiological challenges or changes, including functional activation. Further details of the monitors and their settings are described in sections 2.3, 2.4 and 2.5. Figure 1(a) shows the experimental setup using the TRS-20 as an example with its 30 mm separation optode holder. The studies were conducted in a black enclosure to prevent contamination from external light as shown in Fig. 1(b). The phantom in Figs. 1(c)-1(e) is a clear glass (3 mm thick) enclosure (170 × 50 × 110 mm) that contained diluted Intralipid solution [27, 28], which had a transport scattering coefficient ($\mu_s$') of 10 $cm^{-1}$ and an absorption coefficient ($\mu_a$) of 0.029 $cm^{-1}$ at 760 nm. The measurement was carried out by placing each monitor's probe on the center of the glass window shown in Fig. 1(e) to minimize interference from the phantom walls. The scanning axis (SX) is located approximately 50 mm away from the bottom and top surfaces for the same reason. In addition,

#212653 - $15.00 USD Received 23 May 2014; revised 16 Jul 2014; accepted 16 Jul 2014; published 1 Aug 2014

the inner wall opposite the measurement window and the bottom wall are black to minimize interference.

The local absorber (LA) shown in Fig. 1(f) was made of resin [29] (with 5 × 5 × 10 mm dimensions) and optical properties ($\mu_s$' = 10 cm$^{-1}$ and $\mu_a$ = 0.14 cm$^{-1}$ at 760 nm) similar to soft tissue. The LA was held by a thin metallic rod of 0.5 mm thickness. In our previous study [20], we have demonstrated that this rod did not cause significant effect on the experimental results.

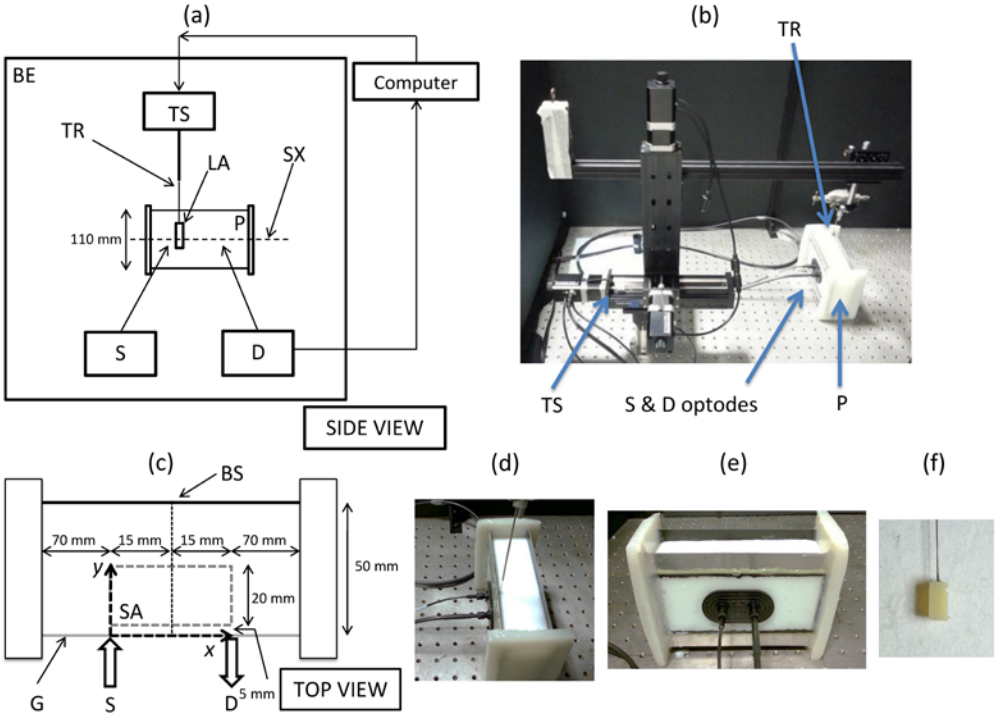


Fig. 1. (a) Schematic diagram of the experimental setup in reflection mode [BE: black enclosure, TS: translation stage, TR: thin metallic rod, LA: local absorber, SX: scanning axis, P: phantom, S: optical source, D: optical detector]; (b) a picture of the setup; (c) Intralipid phantom: distance between S and D is 30 mm [BS: black surface, G: clear glass, y: y-axis distance from G, x: x-axis distance from S, SA: scanning area]; (d) and (e) alternative views of the Intralipid phantom with the TRS-20 optodes' holder, which was attached using the provided adhesive; (f) an image of LA being held by a 0.5 mm TR.

### *2.2. Scanning system and absorption spatial sensitivity map*

The scanning system included three-axis motorized translation stages (Zaber LSR150A) shown in Figs. 1(a) and 1(b) to systematically reposition the LA within the scanning area (SA). The system was controlled automatically by an in-house program (Labview, National Instruments). In Fig. 1(c) the SA is in the same plane as the optodes and is located 5 mm from the phantom wall due to practical reasons. As all three monitors use the diffusion approximation to resolve for tissue oxygenation and it is well known that this approximation is inaccurate when LA is close to the source and boundaries [13]. Hence, the location of SA can help to minimize this inaccuracy. The scanning resolution was 1 mm for both x and y axes. To ensure synchronization, the clocks on the computers controlling the scanning system and all monitors were synchronized and an event marker was initiated at the start of the scanning. The absorption spatial sensitivity $J$ at location ($x$,$y$) in SA is defined by Eq. (1):

#212653 - $15.00 USD Received 23 May 2014; revised 16 Jul 2014; accepted 16 Jul 2014; published 1 Aug 2014

$$J(x,y) = \frac{\mu_a(x,y) - \mu_a^{ref}(x)}{\mu_a^{ref}(x)} \times 100\% = \frac{\Delta\mu_a(x,y)}{\mu_a^{ref}(x)} \times 100\% \quad (1)$$

where $\mu_a(x,y)$ is the average of five $\mu_a$ measurements when LA is at location $(x,y)$ and $\mu_a^{ref}(x)$ is the average of five reference $\mu_a$ measurements. The reference measurement was made using each monitor to derive respective $J(x,y)$ when LA was removed from the liquid phantom.

The reference measurement $\mu_a^{ref}(x)$ is essential to correct the drift in measurement due to the slow sedimentation of Intralipid particles over time. In order to minimize potential large changes in the optical properties, the total experimental time was further reduced by taking only one reference measurement for each $x$ position. $J(x,y)$ is presented as a change in percentage to ensure that reasonable comparison can be made across the varying platforms because only the TRS-20 and ISS Oximeter can measure the absolute value of $\mu_a$. A positive $J(x,y)$ means that the monitor has detected an increase in the measurement and the amount of increment is denoted by its value. For example, 5% sensitivity at $(x,y)$ means when the LA is repositioned from outside the phantom to $(x,y)$, the monitor detects an increment of 5% in measurement. Similarly, a negative $J(x,y)$ denotes a reduction in measurement when LA is introduced into the phantom.

### *2.3. Hamamatsu near infrared oxygenation monitor NIRO-100*

The NIRO-100 system features a single optical source that is capable of outputting three wavelengths (778, 809 and 850 nm) of continuous NIR light and two detectors. This monitor uses the modified Beer-Lambert (MBL) method to resolve for changes in oxy- and deoxy-hemoglobin concentrations in tissue (NIRO-CW) from the changes in attenuation detected across the source and first detector. This monitor also employs SRS [12] (NIRO-SRS) to measure the absolute value of $S_tO_2$, which is called tissue oxygenation index (TOI). This is the ratio of oxygenated hemoglobin to total hemoglobin concentration. NIRO-SRS uses both detectors to detect the slope of the optical attenuation across the detectors. However, this monitor cannot resolve for an absolute value of $\mu_a$. The scaled absolute concentrations of hemoglobin and hence TOI are estimated by using the attenuation slope and the distance between the source and midpoint of the two detectors with the SRS solution to the diffusion equation. Further details on the SRS method can be found in [12, 24].

This monitor was set to have an integration time of two seconds and a total measurement time of ten seconds for every $(x,y)$. The average value of the 5 measurements was used in calculating $J(x,y)$. In addition we used the manufacturer supplied standard fiber bundles that allow the extension of the scanning area to 45 mm (the edge of the second detector) from the center of the source fiber. The monitor was set to output the change in optical density ($\Delta OD$) of the NIRO-CW method and the attenuation slope (OD/cm) of the NIRO-SRS method [12] for the three wavelengths.

The NIRO-CW method uses Eq. (2) to estimate the change in $\mu_a$ ($\Delta\mu_a$ ($cm^{-1}$)), by simply dividing $\Delta OD$ by the optical path length:

$$\Delta\mu_a = \frac{\Delta OD}{PL} \quad (2)$$

where $PL$ is the optical path length, i.e., the product of differential path length factor (DPF) and the distance between the source and first detector spacing (3.7 cm). From Eq. (2), it is obvious that the accuracy and magnitude of the measurement depends on the DPF used because $\Delta\mu_a$ is inversely proportional to the DPF. If the DPF is assumed to be 1, $\Delta\mu_a$ will be scaled and significantly larger than when a DPF of 6.26 for 807 nm (often used for the adult

#212653 - $15.00 USD Received 23 May 2014; revised 16 Jul 2014; accepted 16 Jul 2014; published 1 Aug 2014

head) [30] is used. The phantom is not a realistic head model and so to calculate the optical path length between the optical source and detector for the NIRO-CW method, the relationship $PL = \partial OD/\partial \mu_a = (OD_2 - OD_1)/(\mu_{a,2} - \mu_{a,1})$ was used [11]. An analytical diffusion model of the reflectance $R(\rho)$ was employed [13] to calculate the OD value, i.e., $OD_1 = -\log_{10}[R(d)]$ based on a source detector spacing $d$ = 3.7 cm, $\mu_{a,1}$ = 0.0235 $cm^{-1}$ and $\mu_s$' = 10 $cm^{-1}$. The $OD_2$ value was calculated similarly except $\mu_{a,2}$ was increased by 1%, i.e., $\mu_{a,2}$ = 0.023735 $cm^{-1}$. The resulting PL was 19.5 cm corresponding to a DPF of 5.3 for the phantom.

In order to calculate spatial sensitivity $J_{NIRO\text{-}CW}$ using Eq. (1), $\mu_a^{ref}(x)$ needs to be estimated by other means because the NIRO-CW method is unable to provide an absolute measurement. In this work, the $\mu_a$ of water at its appropriate wavelength [31] has been used for $\mu_a^{ref}(x)$ because the $\mu_a$ of the diluted Intralipid solution can be considered to be that of water in the absence of absorbers [27].

The NIRO-SRS method calculates the scaled $\mu_a$, ($k{\cdot}\mu_a$ ($cm^{-1}$)), from the attenuation slope using the following Eq. (3):

$$k \cdot \mu_a = \frac{1}{3(1 - h \cdot \lambda)} \cdot \left( \ln(10) \cdot \frac{\partial OD}{\partial \rho} - \frac{2}{\rho} \right)^2 \tag{3}$$

where $h$ is the scattering constant ($6.3 \times 10^{-3}$ $cm^{-1}{\cdot}nm^{-1}$), $\lambda$ is the wavelength (nm) and $\rho$ is the distance from the source to the midpoint of the two detectors (4 cm) and $\partial OD/\partial \rho$ is the attenuation slope. Similarly, $J_{NIRO\text{-}SRS}$ is then calculated from both $k{\cdot}\mu_a$ and $k \cdot \mu_a^{ref}$ using Eq. (1) where the constant $k$ is canceled. Preliminaries studies showed comparable results across the wavelengths, thus only the 778 nm results are discussed in detail.

### *2.4. ISS Oximeter*

The ISS Oximeter is a multi-wavelength and multi-distance frequency domain monitor that can resolve for absolute values of optical properties of tissue, i.e., $\mu_a$ and $\mu_s$' and hence calculate oxy- and deoxy-hemoglobin concentrations and estimate $S_tO_2$ (ISS-FD). It modulates the light source intensity at high frequency and measures the reflected modulated light at different distances so slopes of AC, DC and phase measurements can be recorded. These slopes are then used to resolve for $\mu_a$, $\mu_s$', and ultimately $S_tO_2$ [14]. The $\mu_a$ measurement is calculated from the AC and phase measurement, which have been found to be more robust, using the following Eq. (4):

$$\mu_a = \frac{\omega}{2c} \left( \frac{S_\Phi}{S_{AC}} - \frac{S_{AC}}{S_\Phi} \right) \tag{4}$$

where $\omega$ is the angular modulation frequency ($2\pi \times 110$ MHz), $c$ is the speed of light in tissue, and $S_\Phi$ / $S_{AC}$ are the slopes of the phase / AC measurement.

The ISS-FD method used the same integration time and total measurement time of NIRO-100 for the $\mu_a$ measurement. The supplied ISS scanner (part number: 85026, scanner ID: 1050208) was used. This fiber bundles allow two wavelengths measurement at four distances. This particular monitor is capable of outputting four wavelengths of light (690, 750, 790, and 850 nm). Our preliminary studies showed the results of 690 nm were the most stable. The distances of the light sources to detector are 3.55, 3.06, 2.52 and 2.03 cm. Unlike NIRO-100, the ISS-FD method uses multi-distance sources and a single detector. The scanning area of the ISS-FD method extends from the detector to the furthest source. The $J(x,y)$ of the ISS-FD monitor based on changes in intensity has been discussed in the literature [18] so it will not be repeated here.

#212653 - $15.00 USD Received 23 May 2014; revised 16 Jul 2014; accepted 16 Jul 2014; published 1 Aug 2014

The ISS Oximeter requires calibration before measurement and the instrument was set up as it was intended for the study with the same fiber arrangement. After an adequate warming-up period, we used the ISS calibration phantom (part number 75019, ID number 1040824-6; $\mu_a$ = 0.146 $cm^{-1}$ at 690 nm and 0.143 $cm^{-1}$ at 850 nm and $\mu_s$' = 5.1 $cm^{-1}$ at 690 nm and 4.4 $cm^{-1}$ at 850 nm) as it had the largest optical properties differences to our phantom. This is explicitly mentioned in the operation manual, which states that using a calibration phantom that has large differences in optical properties from the target produces more accurate results. The calibration process was then performed using the ISS software with the recommended settings, e.g. appropriate adjustment of gain to ensure adequate intensity detection. Once the calibration process was completed, the post calibration test was performed using standard ISS phantom (part number 75020, ID number 1040827-3; $\mu_a$ = 0.115 $cm^{-1}$ at 690 nm and 0.107 $cm^{-1}$ at 850 nm and $\mu_s$' = 10.9 $cm^{-1}$ at 690 nm and 9.7 $cm^{-1}$ at 850 nm).

*2.5. Hamamatsu time-resolved spectroscopy monitor TRS-20*

The TRS-20 is a new optical tissue monitor from Hamamatsu Photonics K.K. It is a two-channel three-wavelength (760, 800 and 830 nm) time resolved spectroscopy monitor based on the TRS-10 [25] and has been used clinically [26, 32]. The time domain monitor irradiates tissue with pico-second pulses of NIR light. Times of flights of photons are then measured to form a histogram, which is known as the temporal point spread function (TPSF). The TPSF is fitted to a solution of the diffusion equation for a particular geometry with appropriate boundary conditions [13] to estimate the absolute values of $\mu_a$ and $\mu_s$', and subsequently derive hemoglobin concentrations and $S_tO_2$.

The monitor was set for 30 mm optode separation with an integration time of two seconds for the $\mu_a$ measurement. The total time of each measurement was ten seconds and the average value was used. The monitor can also operate using 40 mm separation, however preliminary studies showed inadequate signal-to-noise ratio for an integration time of two seconds, therefore only 30 mm separation results are presented. The scanning area of the TRS-20 method is shown in Fig. 1(c). The TRS-20 software allows the measured TPSF to be fitted to the analytical solutions to the diffusion equation for a reflection geometry using a weighted non-linear least-squares method based on the Levenberg-Marquardt method [33]. In this study, we use the whole TPSF as shown in Fig. 2 and the default semi-infinite slab with zero boundary solution [13], which is described by the following Eq. (5):

$$R(s,t) = (4\pi Dc)^{-3/2} \cdot z_0 \cdot t^{-5/2} \cdot \exp(-\mu_a ct) \cdot \exp\left(-\frac{s^2 + z_0^{\,2}}{4Dct}\right) \qquad (5)$$

where $R(s,t)$ is the reflectance of optode separation $s$ at time $t$; $D$ is the diffusion coefficient = $(3\mu_a + 3\mu_s')^{-1}$; $c$ is the speed of light in tissue; and $z_0$ is the initial scattering length = $(\mu_s')^{-1}$. There are other fitting procedures [6, 34] available, however they require major modifications to the default data analysis; which is beyond the scope of this paper. The value of $\mu_a$ used in the calculation of $J_{TRS\text{-}TD}$ is estimated from the best iterative fit of Eq. (5) to the whole TPSF, which includes correction of the dark count and instrument function. The detail of analysis method of the TRS-20 system is described by Ohmae et al. [35]. Preliminary studies showed that results of 760, 800 and 830 nm wavelengths were similar, so only the 760 nm results are discussed in detail but results of the other wavelengths are briefly summarized.

#212653 - $15.00 USD Received 23 May 2014; revised 16 Jul 2014; accepted 16 Jul 2014; published 1 Aug 2014

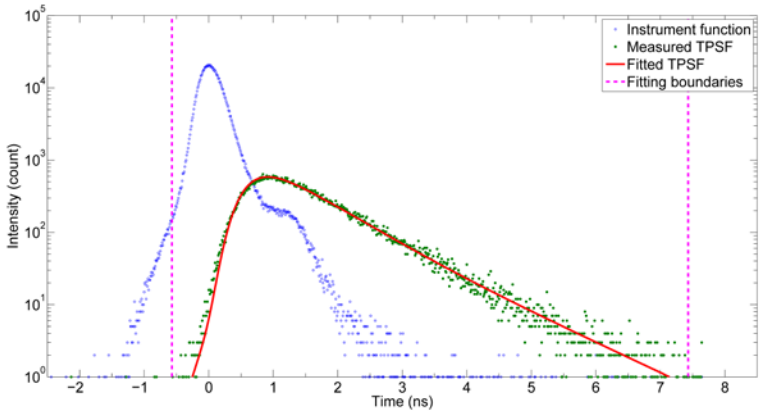


Fig. 2. An example of the TPSF and the fitted TPSF from the Hamamatsu supplied software by fitting the whole TPSF (TRS-20 software automatically sets the peak of the instrument function as t = 0 during calibration).

### *2.6. The relative standard deviation in percentage of spatial sensitivity map*

The relative standard deviation in percentage (%*RSD*) of each sensitivity map is also calculated to indicate the level of signal-to-noise ratio. Recalling that the total measurement period is ten seconds and we sample at an integration time of two seconds, this results in five measurements of $J_{1,2,\ldots,5}$ for every position at ($x$,$y$) within the scanning area. The %*RSD* is derived from the following Eq. (6):

$$\%RSD = median\left\{\frac{\sigma\left(J_{1,2,3,4,5}(x,y)\right)}{\mu\left(J_{1,2,3,4,5}(x,y)\right)}\right\} \tag{6}$$

where σ and μ are the operators for standard deviation and mean, respectively. The median value is used to remove potential outliers.

### *2.7. Mean sensitivity and mean penetration depths*

While $J(x,y)$ can inform on the effects of a highly localized $\mu_a$ change, in some cases a layer wide change in $\mu_a$ may happen. In this case, the mean sensitivity $\langle J(y)\rangle$ at different $y$ depths can be calculated from the average of sensitivity values over $x$ direction.

In addition, the mean penetration depth $\langle y\rangle$ [23] for each monitor can be calculated by Eq. (7):

$$\langle y\rangle = \frac{\sum_i \langle J(y_i)\rangle \cdot y_i}{\sum_i J(y_i)} \tag{7}$$

where $y_i$ = [5, 6, 7, …, 25 mm]. There are two other methods to estimate the penetration depth. For example, it can be estimated as the depth whereby $\langle J(y_i)\rangle$ has reached the background noise level [19] and the LA is so deep that there is no detectable change in $\mu_a$. The penetration depth can also be defined as the depth at which $\langle J(y)\rangle$ is equal to or exceeds a pre-defined threshold [18, 36]. Equation (7) is chosen because it takes into account the depth as the sensitivity values are scaled by the respective depths and normalized.

### *2.8. Regional sensitivity in the superficial layer and the region of interest*

The ideal cerebral monitor would be most sensitive to the cortex and insensitive to the SPL. However, $\mu_a$ changes can occur simultaneously in both regions. It is therefore informative to

#212653 - $15.00 USD Received 23 May 2014; revised 16 Jul 2014; accepted 16 Jul 2014; published 1 Aug 2014

assess the sensitivity of a cerebral monitor to the SPL and to the deeper region, i.e., the region of interest (ROI), separately. To do so, we define (i) the SPL as the region from $y$ = 5 (the starting point of the scanning area) to 12 mm and (ii) the ROI as those from $y$ = 12 mm to the deeper region in the phantom. The thickness of the SPL is based on typical values of the adult human head [7]. For each cerebral monitor, the average sensitivity values in the SPL, $\langle J(SPL)\rangle$ and in the ROI, $\langle J(ROI)\rangle$ are calculated. For a good cerebral monitor, a large $\langle J(ROI)\rangle$ and a small $\langle J(SPL)\rangle$ would be expected.

## 3. Results

The key results are summarized in Table 1. The values reported in the Results and Discussion sections are those from the first wavelength (*) of each monitor. Additional results for other wavelengths are shown to demonstrate their similarity except for the ISS-FD method. The optical probes for the ISS-FD method can be used for two wavelengths measurements (section 2.4) but only the 690 nm results are shown and discussed. This is because the other wavelength failed the manufacturer's post-calibration test on the supplied test phantom.

The $J(x,y)$ of all monitors are shown in Fig. 3 and the color maps are deliberately distinct so that features in the sensitivity maps are obvious. The TRS-TD method is most sensitive to a localized $\mu_a$ change at around $y$ = 20 mm with a maximum $J(x,y)$ of 7.6% in Fig. 3(a). The NIRO-SRS and NIRO-CW methods achieve a maximum $J(x,y)$ of 26.9% and 8.4% at around $y$ = 5 mm and 6 mm respectively near the optical source and detector in Figs. 3(b) and 3(c). The ISS-FD method has the highest maximum $J(x,y)$ of 32.4% near to the optical sources at around y = 9 mm in Fig. 3(d). In terms of signal variability (signal-to-noise ratio), the TRS-TD method has the highest %*RSD* at 46.7%, which is evident when Fig. 3(a) is compared to Figs. 3(b)-3(d). The ISS-FD method has a %*RSD* of 6%. The NIRO-100 monitor has the lowest measurement variations as the NIRO-SRS and NIRO-CW methods achieve %*RSD* of 3% and 2.2% respectively.

**Table 1. Summary of mean penetration depth, mean sensitivity values in the SPL and *ROI*, and %*RSD* of TRS-20 of all monitors with additional results of other wavelengths (values reported refer to the first wavelength* unless otherwise stated and only 690 nm results for ISS-FD due to failure in post calibration test for other wavelength)**

| System-Method | Wavelength (nm) | $\langle y\rangle$ (mm) | $\langle J(SPL)\rangle$ (%) | $\langle J(ROI)\rangle$ (%) | %*RSD* (%) |
|---|---|---|---|---|---|
| NIRO-CW | 778* | 12.5 | 6.1 | 3.2 | 2.2 |
| | 809 | 12.6 | 7.7 | 4.3 | 2.2 |
| | 850 | 12.7 | 3.6 | 2 | 2.1 |
| NIRO-SRS | 778* | 15.3 | 2.5 | 3.4 | 3 |
| | 809 | 15.6 | 2.8 | 4.4 | 2.6 |
| | 850 | 14.9 | 1.9 | 2.3 | 3.7 |
| ISS-FD | 690* | 15.5 | 8.2 | 13 | 6 |
| TRS-TD | 760* | 18 | 1.1 | 3.7 | 46.7 |
| | 800 | 18.8 | 0.8 | 4.6 | 36.6 |
| | 830 | 17.5 | 1.2 | 3 | 55.1 |

#212653 - $15.00 USD Received 23 May 2014; revised 16 Jul 2014; accepted 16 Jul 2014; published 1 Aug 2014

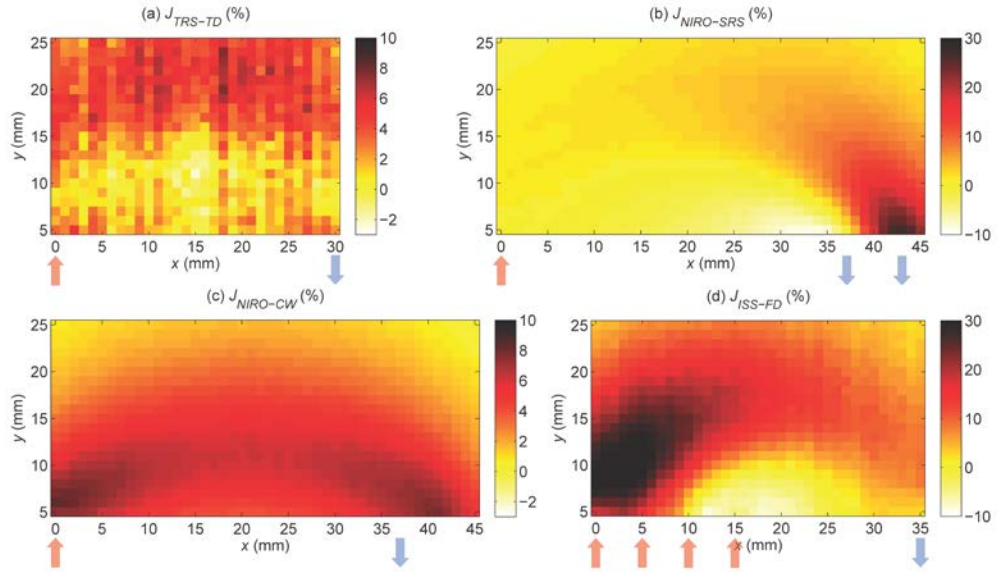


Fig. 3. The spatial sensitivity maps $J(x,y)$* measured with 2 seconds of integration time: (a) TRS-20; (b) NIRO-100 using the SRS method; (c) NIRO-100 using the CW method; (d) ISS Oximeter; TRS-20 has the largest observable measurement variation but is generally more sensitive to deeper regions while other monitors are most sensitive to localized change in the SPL and their measurements have low variability. The color scales of (b) and (d) are deliberately kept distinct from others so the changes can be observable.

The $\langle J(y)\rangle$ of all the monitors are shown in Fig. 4. The TRS-TD method has the maximum $\langle J(y)\rangle$ of 4.9% at $y$ = 21 mm and $\langle y\rangle$ of 18 mm, which is the deepest in comparison to the others. As shown in Table 1, the $\langle y\rangle$ of the NIRO-SRS, NIRO-CW and ISS-FD methods are 15.3, 12.5 and 15.5 mm, respectively. The maximum $\langle J(y)\rangle$ of the NIRO-SRS and NIRO-CW methods are 4.3% and 6.3% respectively and they occur at $y$ = 14 and 8 mm. The highest maximum $\langle J(y)\rangle$ of 16.8% is recorded by the ISS-FD method at 15 mm. The $\langle J(SPL)\rangle$ and $\langle J(ROI)\rangle$ for the TRS-TD, NIRO-SRS, NIRO-CW and ISS-FD methods have been summarized in Table 1. The ISS-FD method records the largest difference ($\langle J(ROI)\rangle$ - $\langle J(SPL)\rangle$) of 4.8% and is followed by the TRS-TD method at 2.6%. The NIRO-SRS and NIRO-CW methods score 0.9% and −2.9% respectively. All the methods are more sensitive to changes in ROI than SPL except the NIRO-CW method as evidenced by the negative 2.9% value. The higher signal variability (%*RSD*) of the TRS-TD measurement in Fig. 3(a) is also observable in Fig. 4 whereby the $\langle J_{TRS-TD}\rangle$ curve shows more variability than others.

#212653 - $15.00 USD Received 23 May 2014; revised 16 Jul 2014; accepted 16 Jul 2014; published 1 Aug 2014

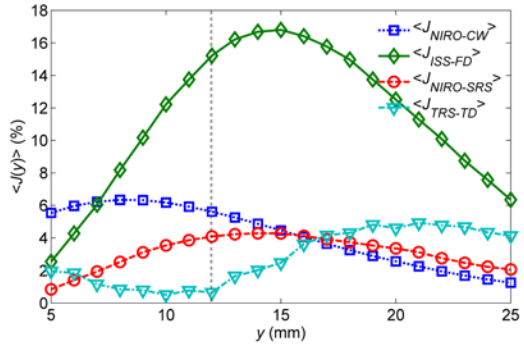


Fig. 4. The <*J*(*y*)>* at different depths: the ISS-FD method has the highest <*J(y)*> across *y* and every method is generally less sensitive to the SPL change in $\mu_a$ except the NIRO-CW method (the dashed grey line shows the boundary of the SPL).

The %*RSD* of the TRS-TD method in Table 1 is the highest among all the monitors tested as demonstrated by the noisy sensitivity map in Fig. 3(a). It implies that the two second integration time is not adequate. The same study has been repeated and the integration time was increased to five and ten seconds. The results are summarized in Table 2 with additional results of other wavelengths. As before, the values reported in the Results and Discussion sections are those from the first wavelength (*) unless otherwise stated. The sensitivity maps of using longer integration times are shown in Fig. 5 and the improvements are obvious. The %*RSD*s of using five and ten seconds are 28.6% and 17.2% respectively. They are still higher than the %*RSD* of NIRO-100 and ISS-FD but are a significant improvement from using two seconds. They also improve the visibility of the slightly higher *J*(*x*,*y*) values near the optical source and detectors in Fig. 5. The maximum values of $J_{TRS\text{-}TD\text{-}5s}$ (7.2%) and $J_{TRS\text{-}TD\text{-}10s}$ (7.6%) occur at *y* = 23 and 20 mm respectively. These values are consistent with the two-second integration result, which is discussed earlier.

**Table 2. Summary of mean penetration depth, mean sensitivity values in the SPL and ROI, and %*RSD* of TRS-20 for 2, 5 and 10 seconds integration time (values reported refer to the first wavelength* results unless otherwise stated)**

| Integration time (s) | Wavelength (nm) | <*y*> (mm) | <*J*(SPL)> (%) | <*J*(ROI)> (%) | %*RSD* (%) |
|---|---|---|---|---|---|
| 2 | 760* | 18 | 1.1 | 3.7 | 46.7 |
| | 800 | 18.8 | 0.8 | 4.6 | 36.6 |
| | 830 | 17.5 | 1.2 | 3 | 55.1 |
| 5 | 760* | 18.7 | 0.8 | 4.1 | 28.6 |
| | 800 | 19.3 | 0.5 | 5 | 25.1 |
| | 830 | 18.2 | 0.9 | 3.3 | 37.7 |
| 10 | 760* | 20.3 | –0.6 | 4.3 | 17.2 |
| | 800 | 20.2 | –0.5 | 5.7 | 13 |
| | 830 | 19.3 | 0 | 3.5 | 21 |

#212653 - $15.00 USD Received 23 May 2014; revised 16 Jul 2014; accepted 16 Jul 2014; published 1 Aug 2014

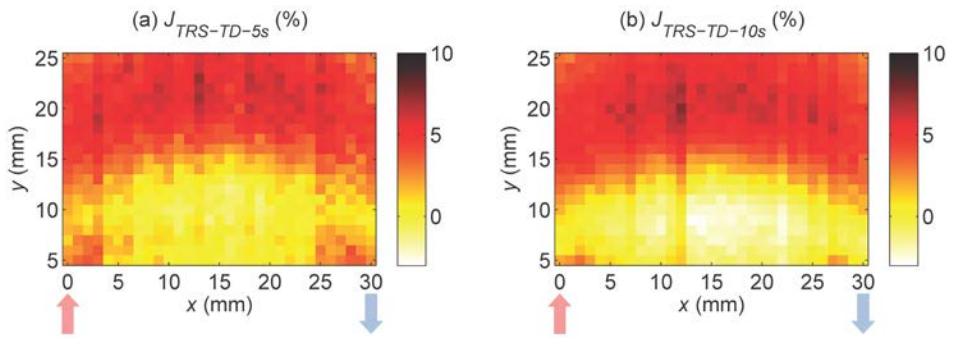


Fig. 5. The spatial sensitivity map of the 760nm of the TRS-20 using an integration time of: (a) 5 and (b) 10 seconds; they show considerably improvement in %*RSD* (28.6% and 17.2% respectively) and the monitor is consistently most sensitive to deeper regions than SPL.

It is interesting to observe that the TRS-TD method is not the most sensitive when the $\mu_a$ change is near the optical source and detector especially when compared to other monitors. There are observable slight increases in $J(x,y)$ in these SPL regions but the highest values are consistently located at $y$ = 20 mm, even when the integration time is not sufficient. Time resolved monitors like TRS-TD measure $\mu_a$ and $\mu_s$ from the shape of the recorded TPSF by curve fitting. The results here imply that when $\mu_a$ change is in the SPL, there are minimal changes to the shape of the TPSF and therefore the fitted $\mu_a$ and $\mu_s$. On the other hand, when the localized $\mu_a$ change is deeper, the result is a larger change in both the shape of TPSF and the fitted $\mu_a$ and $\mu_s$. In other words, the fitting process of the TRS-TD method may inherently offer the same effect as the hardware time-gating of late arriving photons and suppression of the early arriving photons, which has been shown to improve depth selectivity [34]. This time-gating method has been further improved numerically and validated by Zuccelli et al. [37]. However, even using a 10 seconds integration time, the %*RSD* of TRS-TD method is still the worst amongst the monitors.

The corresponding $\langle J(y) \rangle$ results are shown in Fig. 6. The maximum $\langle J(y) \rangle$ values are fairly similar to the result of using two seconds integration time, which are 5.5% and 5.7% respectively for five and ten seconds. The slight increase can be attributed to the lower %*RSD*. These maxima are found at $y$ = 21 and 20 mm respectively, which are highly similar to the result ($y$ = 21 mm) of two seconds integration time. $\langle J_{TRS\text{-}TD\text{-}5s}(\mathrm{ROI}) \rangle$ is 4.1% and $\langle J_{TRS\text{-}TD\text{-}5s}(SPL) \rangle$ is 0.8% resulting in a difference of 3.3%, which is an improvement from the 2.6% result of two seconds integration time. $\langle J_{TRS\text{-}TD\text{-}10s}(\mathrm{ROI}) \rangle$ is 4.3% and $\langle J_{TRS\text{-}TD\text{-}10s}(\mathrm{SPL}) \rangle$ is –0.6%, which equates to a difference of 4.9% (equal to the 4.9% relative sensitivity of ISS-FD, which is highest when two seconds integration time is used). The negative value is intriguing because it means TRS-TD suppresses the detected value of $\mu_a$ when there is a layer change of $\mu_a$ in SPL. These findings are reaffirmed by $\langle y \rangle$, which has improved from 18 mm when using a two seconds integration time to 18.7 and 20.3 mm respectively when five and ten seconds are used. So, using a longer integration time will not only reduce the amount of variability in measurement, it also lowers $\langle J(SPL) \rangle$ while increasing $\langle J(ROI) \rangle$. Based on these results with adequate integration time, there may not be a need for additional short-distance measurements [38] to account for regional SPL contamination. However, using a longer integration time compromises the scope of potential clinical applications that the monitor can be utilized for.

#212653 - $15.00 USD Received 23 May 2014; revised 16 Jul 2014; accepted 16 Jul 2014; published 1 Aug 2014

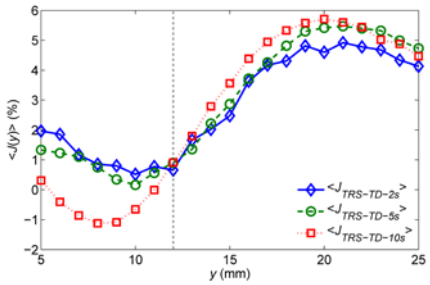


Fig. 6. The <*J*(*y*)> profiles* of the TRS-TD method for integration time = (a) 2, (b) 5 and (c) 10 seconds; and they show minimal <*J*(*SPL*)> and higher sensitivity in deeper regions (the dashed grey line shows the boundary of the SPL).

## 4. Discussions

The TRS-TD demonstrated the deepest mean penetration depth followed by the ISS-FD and then the NIRO-SRS and CW methods. The NIRO-CW, NIRO-SRS and ISS-FD are sensitive to localized absorption changes near the optical source and detector. The ISS-FD has the highest absolute sensitivity and mean sensitivity in both SPL and ROI. The mean sensitivity of each method, which can also be regarded as the method's response to a layer-wide change in $\mu_a$, shows that all the methods, except the NIRO-CW method, are generally more responsive to layer $\mu_a$ changes in the deeper regions. The NIRO-CW method is more sensitive to the SPL than the ROI. Finally the TRS-TD measurement has the poorest signal to noise ratio even when five times the integration time of other monitors is used.

### *4.1. Negative sensitivity values*

The negative *J*(*x*,*y*) values can be observed for the TRS-TD, NIRO-SRS and ISS-FD methods, which means that the measured $\mu_a$ (when the LA is in the phantom) became smaller than the reference $\mu_a$ (when the LA is withdrawn from the phantom) according to Eq. (1). Only the NIRO-CW method shows all positive sensitivity values. The negative *J*(*x*,*y*) of TRS-TD is likely due to the fitting schedule. For the NIRO-SRS method, the scaled $\mu_a$ is derived from the attenuation slope according to Eq. (3); and if the scaled $\mu_a$ decreases, the attenuation slope decreases too. When the LA is withdrawn from the medium, the first detector (D1) detects a smaller attenuation (higher intensity) than the second detector (D2) because D1 is closer to the source. If the LA is relocated near D1, the attenuation at D1 increases and results in an increase in the attenuation difference, Δ*OD*, between D1 and D2. This causes the attenuation slope to decrease compared to the reference value. The attenuation slope can even become negative if the $\mu_a$ of the LA is significantly larger. When the LA is positioned closer to D2, the attenuation slope becomes larger than the reference attenuation slope, resulting in a positive *J*(*x*,*y*). These negative and positive values are averaged in the calculation of <*J*(*y*)> over the *x*-direction for each value of *y*. The <$J_{NIRO\text{-}SRS}$(*SPL*)> becomes small indicating that the NIRO-SRS method is relatively insensitive to $\mu_a$ layer-wide changes in the SPL. Similar phenomena can be observed in <$J_{ISS\text{-}FD}$(*y*)> and <$J_{ISS\text{-}FD}$(*SPL*)> because the ISS-FD method also uses slopes of AC, DC and phase for $\mu_a$ measurement. The difference is that these negative and positive *J*(*x*,*y*) values occur near the multi-distance sources.

### *4.2. Effects of scalp blood flow on cerebral oxygenation monitoring*

Contaminations from scalp blood flow changes on brain oxygenation monitoring are well discussed in the literature [1–3]. It is often assumed that the blood flow measured in one area of the scalp can be representative of the whole, an assumption that we have recently challenged [9]. Al-Rawi et al. [39] used the NIRO-300, which uses the same methods as the NIRO-100 monitor to measure TOI and changes in oxy- and deoxy-hemoglobin concentrations to compare the effects of intracranial (ROI) and extracranial (scalp) changes on

#212653 - $15.00 USD Received 23 May 2014; revised 16 Jul 2014; accepted 16 Jul 2014; published 1 Aug 2014

TOI. They showed that the TOI is not affected by scalp changes, which can be explained by the NIRO-SRS method's $\langle J(y)\rangle$ in Fig. 4. The scalp is typically a few millimeters thick and at $y$ = 5 mm, $\langle J_{NIRO\text{-}SRS}\rangle$ is about 0.85% and $\langle J_{NIRO\text{-}SRS}(ROI)\rangle$ is 3.4% resulting in a ratio $\langle J_{NIRO\text{-}SRS}(y = 5 \text{ mm})\rangle/\langle J_{NIRO\text{-}SRS}(ROI)\rangle$ of 25%; which means that the SPL contributes approximately 25% to the measurement if concurrent absorption changes were to occur. The curve of $\langle J_{NIRO\text{-}SRS}\rangle$ shows that if a layer-wide change occurs in the scalp, it will not have a large impact on the measurement. Al-Rawi reported intracranial sensitivity of 87.5% and extracranial sensitivity of 13%, resulting in a ratio of extra-to-intracranial sensitivity of 14.9%, which is fairly similar to that of $\langle J_{NIRO\text{-}SRS}(y = 5 \text{ mm})\rangle/\langle J_{NIRO\text{-}SRS}(ROI)\rangle$ in spite of the differences in geometry and conditions. However, we have recently shown with MRI angiography [9] that changes in scalp blood flow are regional and largely dependent on highly localized deep draining veins in the scalp. In this case, the only monitor that has a minimal response to a localized change near $y$ = 5 mm is the TRS-TD method according to Fig. 3. However, this may have resulted in the poorer %*RSD* as it has been shown in the literature that excluding the tail of TPSF may improve signal to noise ratio. This requires future investigation for verification.

### *4.3. Comparison to previous findings*

The $J(x,y)$ of NIRO-CW in Fig. 3(c) and NIRO-SRS in Fig. 3(b) can be compared to our previous findings [20], which were validated by computer simulation [40]. They are briefly described in the Introduction section. There are some methodological differences between our previous and current studies. In our previous study, the $J(x,y)$ have been calculated from the intensity based measurements using the single source-detector (SSD), spatially resolved (SR) and acousto-optic (AO) configurations. In this paper, $J(x,y)$ is derived from $\mu_a$ measurement. Furthermore, the derivation of the spatial sensitivity of the SSD and AO methods was different and the $\mu_a$ of the LA used in the previous study was considerably larger than the one used in the current study.

The current NIRO-CW result agrees with our previous SSD results, which is not surprising given that both depend on the changes in intensity. Both results depict the classic 'banana' shape of photon path length distribution and the most sensitive regions are close to the optical source and detector. These two methods are also more sensitive to $\mu_a$ changes in the SPL than in deeper regions as illustrated by their respective $\langle J(y)\rangle$. Besides the difference in $\mu_a$ of the LA, the source detector separation is also different. The NIRO-CW method has a slightly larger separation (37 mm from source to the center of first detector) than the SSD method (30 mm). So $\langle y\rangle$ of the NIRO-CW method is slightly longer at 12.5 mm compared to that of the SSD method (11.4 mm). Unlike the NIRO-SRS method used in this paper, our previous results demonstrated more sensitivity to a layer change in the SPL than in the ROI; which can be attributed to the difference in the scanning area. The scanning area of the SR method extended from the source to the center of the three-detector setup and the scanning area of the NIRO-SRS method extends from the center of the source to the further edge of the second (last) detector. In the derivation of mean sensitivity for the NIRO-SRS method, the positive sensitivities are averaged with the negative sensitivities, which in turn results in a low mean sensitivity value in the SPL. For the SR method, the high positive $\langle J_{SR}\rangle$ values were not averaged by the corresponding negative sensitivities because the scanning area only extended to the midpoint of the detectors; hence resulting in the seemingly high SPL sensitivity.

Similar to the NIRO-CW method, the AO method is most sensitive to localized changes near the optical source and detector. However, its $\langle J(y)\rangle$ suggests that this method is generally insensitive to layer changes in the SPL, depending on the location of focused ultrasound. By refocusing the ultrasound deeper in the phantom, the AO method can achieve a $\langle y\rangle$ up to 15.8 mm; which is better than both the NIRO-SRS and ISS-FD methods. Only the TRS-TD method has a deeper $\langle y\rangle$, which is 18 mm.

#212653 - $15.00 USD Received 23 May 2014; revised 16 Jul 2014; accepted 16 Jul 2014; published 1 Aug 2014

*4.4. Limitation of the perturbation method*

Typical chromophore concentration changes, for example during functional activation studies, are typically in the order of few micro-molar and the resulting change in $\mu_a$ is small. Assuming an increase of 4 μM in oxy-hemoglobin and a decrease of 1 μM in deoxy-hemoglobin [36], the resulting change in $\mu_a$ is 0.0018 $cm^{-1}$ at 760 nm as estimated using the UCL specific absorption spectra [31]. Such change is miniscule hence poor signal to noise ratio [4, 6] is a problem in NIRS studies. Higher absorption changes (contrast) have been used before in other numerical (simulation) and experimental perturbation studies, for example $\mu_a$ changes of 0.3 and 3.9 $cm^{-1}$ at 800 nm [41, 42] used a $\mu_a$ that is 17.5 times (1.75 $cm^{-1}$ at 605 nm) larger than the background $\mu_a$; and [43, 44] used a $\mu_a$ contrast of 0.15 $cm^{-1}$. Our previous study [20] used a 'black' LA ($\mu_a$ = 40.3 $cm^{-1}$) and the results were verified by Monte Carlo simulation [40]. Besides the absorption change, the larger perturbation size can also affect the accuracy of perturbation study [45]. The LA (5 × 5 × 10 mm) is smaller in comparison to [36] and [43] where dimensions of 10.6 × 10.6 × 10.6 and 10 × 10 × 10 mm were used respectively. Hence, the 0.1 $cm^{-1}$ difference of $\mu_a$ between the phantom and small perturbation LA was used to ensure adequate signal to noise ratio in our measurements.

The first wavelengths of the NIRO-100 (778 nm) and TRS-20 (760 nm) are similar. The $\mu_a$ of LA and the Intralipid phantom are 0.14 and 0.03 $cm^{-1}$ at 760 nm respectively. However, the wavelength used for the ISS Oximeter measurements was 690 nm and the $\mu_a$ of LA is 0.097 $cm^{-1}$ at 690 nm measured by the ISS Oximeter. The $\mu_a$ of Intralipid phantom at 690 nm is 0.005 $cm^{-1}$. This means the amount of change in $\mu_a$ (when LA is outside and in the phantom) detectable by the ISS Oximeter at 690 nm is similar to that measured by other systems at 760 or 778 nm.

Furthermore, the experiments were conducted using a homogeneous phantom, which was not realistic head geometry and did not possess a $\mu_a$ that was similar to the brain. Therefore, the value of $J(x,y)$ is arbitrary and should not be taken as a monitor's cerebral saturation sensitivity. It is only useful when it is compared to another value, which is measured by the same perturbation method using similar phantom. The same caution applies to $\langle J(y) \rangle$ and $\langle y \rangle$. For example, a monitor that has a $\langle y \rangle$ of 15 mm will not probe 15 mm deep in the human head. However, it is not improbable for that monitor to probe deeper into the head than a monitor that has a $\langle y \rangle$ of 12 mm. Hence, the former has better likelihood of measuring ROI than SPL. In addition, the sensitivity measurement is not susceptible to potential inaccuracy in the resolved absorption that could be caused by partial volume effects and cross talk, which have been shown to be important issues in NIRS measurements [15, 46–50]. They are beyond the scope of the aims of this paper but could guide future work to investigate the spatial sensitivity and/or the measurement accuracy of these monitors by using a phantom that features a more realistic head geometry than the phantom used in this study; for example a two-layer head model that is proposed in the literature [46, 49, 50].

Ideally, the scanning area should extend from the source and detector to the point whereby there is no detectable $\mu_a$ change so that there is minimal adverse effect on the calculation of mean sensitivity discussed in section 4.3. The chosen scanning area is a compromise to avoid an extended experimental time that may adversely affect the optical properties of the Intralipid solution due to sedimentation. Furthermore, the scanning starts at $y$ = 5 mm instead of 0 mm due to practical reasons; this will affect the calculation of $\langle y \rangle$. However the sensitivity values in this shallow region are smaller (Fig. 4) and they are multiplied by a smaller $y$ (1 to 5 mm). Similarly, the current mean sensitivity is derived from a two-dimensional slice of spatial sensitivity map whereby a three-dimensional derivation is more appropriate. Both simulation and experimental studies [18, 23] have shown that two-dimensional approach can still be a good representation of the overall penetration depth of the systems.

#212653 - $15.00 USD Received 23 May 2014; revised 16 Jul 2014; accepted 16 Jul 2014; published 1 Aug 2014

### *4.5. Usability and data collection*

Usability is a factor that is often omitted in the reviews of NIRS instrumentation. For these studies we considered the complexity of setup procedure required from powering on to start of measurement and data collection. The observations are based on the specific monitors that we used in this study and future generations may evolve and improve on their current specifications and performance. All three monitors require similar warm-up time for temperature stability. The NIRO-100 is a stand-alone monitor and it is the most convenient to set up, calibrate and use. The next most straightforward is the TRS-20, which requires a laptop computer to operate and has a relatively straightforward calibration process. The ISS Oximeter requires a desktop computer and its setup time is longest due to the calibration and verification processes that require specific measurements on test phantoms. Furthermore, the setup arrangement of the fibers' between the calibration and actual measurement must not change significantly.

NIRS monitors are often used with other medical monitors and in some clinical applications they are required to be synchronized. The available options for all of the three monitors used are synchronizing the system clock or inserting event markers manually. These options may be neither convenient nor accurate when the operator needs to control multiple instruments at the same time.

The NIRO-100 has a limit of recordable data points depending on the sampling rate of measurement. The limit of the NIRO-100 can be mitigated by setting it to output the data via the serial port. The TRS-20 has a maximum limit of 5000 data point. The maximum ISS Oximeter data log file size is limited by the available storage space in the computer and the version of the operating system.

## 5. Conclusions

Three cerebral oxygenation monitors have been investigated and compared in terms of their sensitivities to local or layer-wide $\mu_a$ changes and the mean penetration depth $\langle y \rangle$. The TRS-20 has the deepest $\langle y \rangle$ of nearly 20 mm and is least susceptible to local and layer-wide SPL $\mu_a$ changes. However, it requires a longer integration time of more than five seconds to achieve an acceptable level of measurement variability in comparison to the NIRO-100 (lowest) and the ISS Oximeter. This factor can possibly limit the scope of clinical application of the TRS-20. Furthermore, the signal to noise ratio of the TRS-20 is the poorest even when longer integration time is used.

Both the NIRO-100 and the ISS Oximeter are sensitive to localized changes in the SPL close to the optical sources and detectors but not when these changes are layer-wide. The NIRO-CW method is the only method that is adversely influenced by local and layer-wide SPL changes and it also has the most shallow mean penetration depth. The ISS Oximeter has the highest absolute sensitivity in deeper regions, followed by the TRS-20 and the NIRO-100. In terms of the relative sensitivity between SPL and ROI, the TRS-20 is similar to the ISS Oximeter when an extended integration time is used. Overall, the ISS Oximeter has the highest sensitivity in both shallow and deep regions.

## Acknowledgments

The NIRO-100 and TRS-20 monitors used in this study were supplied by Hamamatsu Photonics K. K. We thank Susumu Suzuki (Hamamatsu Photonics K.K.) for his assistance in using the NIRO-100. We thank Hiroaki Suzuki (Hamamatsu Photonics K.K.) for his assistance in using the TRS-20. We thank Dennis Hueber (ISS Inc.) for his assistance in using the ISS Oximeter. Sonny Gunadi was supported by Hamamatsu Photonics K.K.; Ilias Tachtsidis was supported by the Wellcome Trust (088429/Z/09/Z) and Terence Leung was supported by EPSRC (EP/G005036/1).

#212653 - $15.00 USD Received 23 May 2014; revised 16 Jul 2014; accepted 16 Jul 2014; published 1 Aug 2014